Towards an optimal model for a bistable nematic liquid crystal display device

L. J. Cummings, C. Cai & L. Kondic

Journal of Engineering Mathematics

ISSN 0022-0833
Volume 80
Number 1

J Eng Math (2013) 80:21-38
DOI 10.1007/s10665-012-9607-4

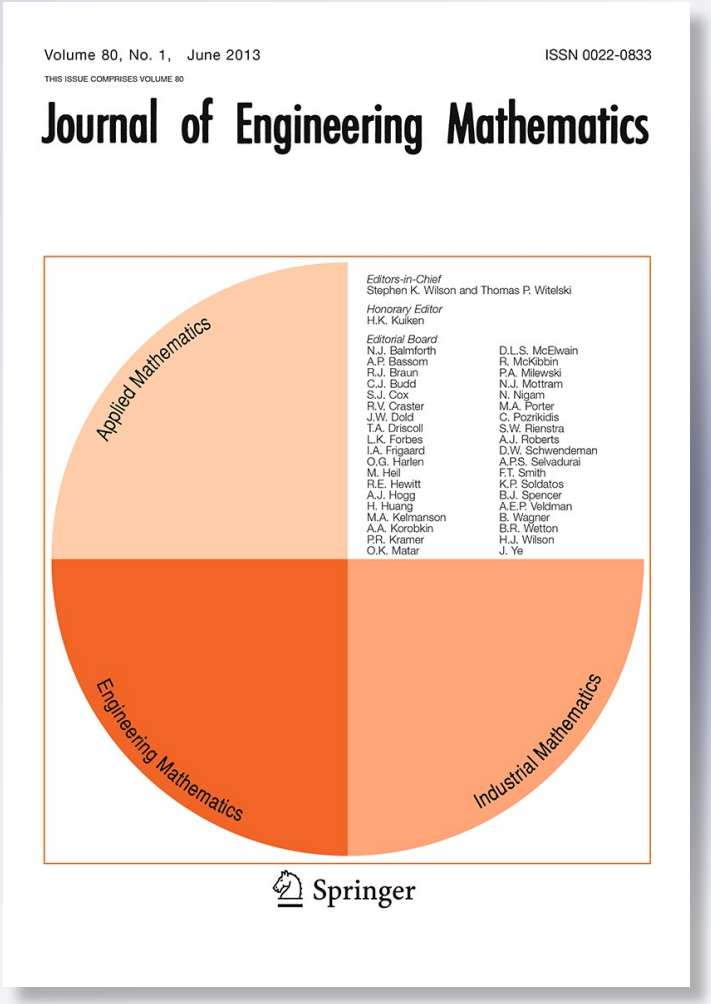

Springer

J Eng Math (2013) 80:21–38
DOI 10.1007/s10665-012-9607-4

Towards an optimal model for a bistable nematic liquid crystal display device

L. J. Cummings · C. Cai · L. Kondic

Received: 7 September 2011 / Accepted: 16 November 2012 / Published online: 13 March 2013

Abstract Bistable liquid crystal displays offer the potential for considerable power savings compared with conventional (monostable) LCDs. The existence of two stable field-free states that are optically distinct means that contrast can be maintained in a display without an externally applied electric field. An applied field is required only to switch the device from one state to the other, as needed. In this paper we examine a theoretical model of a possible bistable device, originally proposed by Cummings and Richardson (Euro J Appl Math 17:435–463 2006), and explore means by which it may be optimized, in terms of optical contrast, manufacturing considerations, switching field strength, and switching times. The compromises inherent in these conflicting design criteria are discussed.

Keywords Bistability · Liquid crystal display · Nematic

1 Introduction

With the current sustained demand for portable interactive electronic devices with displays (phones, e-readers, netbooks, music players, etc.), there is considerable interest in methods by which their power consumption may be reduced. Lower power consumption gives improved battery lifetimes and also allows smaller batteries to be used, offering increased portability. In many small electronic devices the screen is responsible for a sizeable portion of the power consumption; therefore, research into low-power electronic displays is potentially very lucrative. Most modern e-readers use "e-ink" (or closely-related) technology [1], which uses very little power; but most portable phones, netbooks, and music players use conventional liquid crystal display (LCD) technology in their displays, which has higher power consumption but better optical properties.

E-ink technology utilizes a suspension of tiny spherical microcapsules dispersed in a clear carrier fluid. Each microcapsule contains positively charged white particles and negatively charged black ones. In a DC electric field, all white particles will move to one side of the microcapsules, whereas the black ones move to the opposite side. If the electric field direction is reversed, then so is the motion of white and black particles in the microcapsule. Hence display contrast can be controlled by applying fields of appropriate polarities in different portions of the

L. J. Cummings (✉) · C. Cai · L. Kondic
Department of Mathematical Sciences and Center for Applied Mathematics and Statistics,
New Jersey Institute of Technology, Newark NJ 07102, USA
e-mail: linda.cummings@njit.edu

screen (pixels). Moreover, once the field is removed, the particles stay where they are within the microcapsule, so that a field is required only to change the state of the display. This is an example of simple bistable technology since the microcapsules remain stable in a given state until an electric field is applied to change the state; there are two such stable states.

Conventional LCD technology, on the other hand, requires continuous application of an electric field. At the simplest level, a thin layer of nematic liquid crystal (NLC) is sandwiched between two plates and placed between crossed polarizers. The NLC is birefringent: depending on its molecular orientation, it can rotate the plane of polarized light. The molecular orientation within the NLC can be controlled by application of an electric field across the layer (its molecules, which are like little rods, align in an applied field). Typically, with the molecules aligned, the polarized light passing through the first polarizer is not rotated as it passes through the NLC layer. Thus, it cannot pass through the second, crossed, polarizer. With no applied field, however, the molecular orientation within the layer is different (dictated solely by boundary effects now, rather than the electric field); the polarized light is rotated as it passes through the NLC layer and can pass through the second crossed polarizer. These two states are therefore optically distinct when light is passed through (the first will be dark, the second bright) and form the basis of an electronic display. However, the electric field must be "on" to maintain the contrast between neighboring pixels, meaning that such displays are energetically expensive.

One way to reduce the power consumption of an LCD device is to design it so that there are two stable states for the molecular orientation in the absence of an applied electric field. Provided these stable states are optically distinct and may be switched from one to the other by transient application of an electric field, power consumption could rival that of e-ink technology, yet with superior optical properties. In this paper, we consider one possible theoretical design for such a bistable nematic LCD device. The design, which has yet to be verified experimentally, follows earlier work by Cummings and Richardson [2], which relies on the premise that the bounding surfaces can be engineered so as to control the preferred molecular orientation of the nematic molecules (the reasonableness of this premise is argued subsequently in Sect. 2). In that paper, however, only a limited subset of possible anchoring conditions was considered; bistability (with two-way switching) was found to be possible, but only under rather restrictive conditions (discussed subsequently), which would make the device challenging to build. Here we broaden our design parameters to alleviate these restrictions, and we further address the issue of which among the family of possible designs is the "best" according to certain metrics that we devise. These improvements of the original design should bring it much closer to physical realization.

The paper is laid out as follows. In Sect. 2 we introduce the key dependent variables and the basic mathematical model. We first consider the steady-state model before generalizing to the time-dependent case. Section 3 addresses the bistability at zero field, outlines our criteria for deciding whether one device is better than another, and derives the "benefit function" based on these criteria. Section 4 describes the simulated annealing numerical approach taken to optimize this benefit function and carries out the optimization in several stages. Finally, in Sect. 5, we draw our conclusions.

2 Mathematical modeling: basic device design

The basic setup is a layer of NLC, sandwiched between parallel bounding surfaces at $z^* = 0$ and $z^* = h^*$. Star superscripts will be used throughout to denote dimensional quantities and will be dropped when we nondimensionalize. The molecules of the NLC are rodlike, which imparts anisotropy. The molecules like to align locally, which may be modeled by associating an elastic energy with any deviations from uniform alignment (Sect. 2.1 below). The local average molecular orientation is described by a director field $\boldsymbol{n}$, a unit vector, and in our simple model we assume that this director field is constrained to lie in a plane, the (x^*, z^*)-plane. We assume further that properties do not vary in the x^*-direction, thus the director field may be expressed in terms of a single angle $\theta(z^*, t^*)$,

$$\boldsymbol{n} = (\sin\theta, 0, \cos\theta), \tag{1}$$

and the electric field throughout the NLC layer is uniform: $\boldsymbol{E}^* = E^*(0, 0, 1)$. In reality, there is interaction between the electric field and the NLC, so that even if $\boldsymbol{E}^*$ is uniform outside the layer, it will vary across the layer. A more

careful treatment would take this into account; however, we do not anticipate significant variation of the field across the layer, and we expect the uniform field assumption is sufficient for the proof-of-principle investigation herein. (Recall that in any case, an electric field is utilized only to switch the display from one state to the other.)

Since we require bistability in the absence of an applied field, conditions at the bounding surfaces $z^* = 0,\ h^*$ are key. At an interface between an NLC and a solid boundary, the NLC molecules have some preferred orientation. This is known as anchoring. The anchoring pretilt angle (denoted by α in our model, the preferred value of θ at either interface) may be controlled by a variety of surface treatments; for example, mechanical or chemical treatments, nanopatterning, and surface irradiation have all been shown to produce certain desired anchoring angles [3–13] with a high degree of control. The strength A^* of the anchoring may also be controlled to some extent [9,10,14,15] by similar methods. As evidenced by these cited works, advances in the degree of control attainable are continually being made and, while not quite yet a reality, "bespoke surfaces" with desired anchoring properties are becoming a real possibility for the near future. We shall therefore assume that surface anchoring angles and strengths are adjustable parameters in the modeling, within a range of physically realistic values.

We begin by considering the equations and boundary conditions when time dependence is neglected (this would be the case if, for example, the applied field was varied only slowly).

2.1 Steady-state energetics

The free energy of the liquid crystal layer, in the presence of an applied electric field and with specified anchoring conditions at each bounding surface, has several contributions. The bulk free energy density consists of elastic, dielectric, and flexoelectric contributions W_{e}^*, W_{d}^*, W_{f}^*, and in our 2D model with the uniform field assumption these are given by

$$
\begin{aligned}
2W_{\mathrm{e}}^* &= K_1^*(\nabla^* \cdot \boldsymbol{n})^2 + K_3^*((\nabla^* \times \boldsymbol{n}) \times \boldsymbol{n})^2,\\
2W_{\mathrm{d}}^* &= -\varepsilon_0^*(\varepsilon_\parallel - \varepsilon_\perp)(\boldsymbol{n} \cdot \boldsymbol{E}^*)^2,\\
W_{\mathrm{f}}^* &= -\boldsymbol{E}^* \cdot (e_1^*(\nabla^* \cdot \boldsymbol{n})\boldsymbol{n} + e_3^*(\nabla^* \times \boldsymbol{n}) \times \boldsymbol{n}),
\end{aligned}
$$

where K_1^* and K_3^* are elastic constants, ε_0^* is the permittivity of free space, $\varepsilon_\parallel$ and $\varepsilon_\perp$ are the relative dielectric permittivities parallel and perpendicular to the long axis of the nematic molecules, and e_1^* and e_3^* are flexoelectric constants [16–18]. With the director field $\boldsymbol{n}$ as given by (1), with $\theta = \theta(z^*)$, and the common simplifying assumption $K_1^* = K_3^* = K^*$, the total bulk free energy density $W^* = W_{\mathrm{e}}^* + W_{\mathrm{d}}^* + W_{\mathrm{f}}^*$ simplifies. Introducing the nondimensional forms $W = K^* W^*/h^{*2}$ and $z = z^*/h^*$,

$$
W = \frac{\theta_z^2}{2} - \mathcal{D}\cos^2\theta + \frac{\mathcal{F}\theta_z}{2}\sin 2\theta, \tag{2}
$$

where

$$
\mathcal{D} = \frac{h^{*2}E^{*2}\varepsilon_0^*(\varepsilon_\parallel - \varepsilon_\perp)}{2K^*}, \quad \mathcal{F} = \frac{h^*E^*(e_1^* + e_3^*)}{K^*}, \tag{3}
$$

are dimensionless constants. With *representative* characteristic values (not intended to be absolute in what follows; a certain amount of variation about these values is possible)

$$
h^* \approx 1\,\mu\mathrm{m}, \quad E^* \approx 1\mathrm{V}\,\mu\mathrm{m}^{-1}, \quad e_1^* + e_3^* \approx 5 \times 10^{-11}\,\mathrm{C\,m}^{-1}, \quad K^* \approx 1 \times 10^{-11}\mathrm{N}, \quad \varepsilon_\parallel - \varepsilon_\perp \approx 5,
$$

[19–21] both $\mathcal{D}$ and $\mathcal{F}$ are $O(1)$. Note that these parameters are not independent; the ratio

$$
\Upsilon = \frac{\mathcal{F}^2}{\mathcal{D}} = \frac{2(e_1^* + e_3^*)^2}{K^*\varepsilon_0^*(\varepsilon_\parallel - \varepsilon_\perp)} \tag{4}
$$

is a material parameter, independent of device design, and so must remain fixed. We consider the case in which the dielectric anisotropy $\varepsilon_\parallel - \varepsilon_\perp > 0$, so that $\mathcal{D} > 0$ always (this means that an applied field acts to align molecules with the field, rather than perpendicular to it). The parameter $\mathcal{F}$, characterizing the dimensionless strength of the

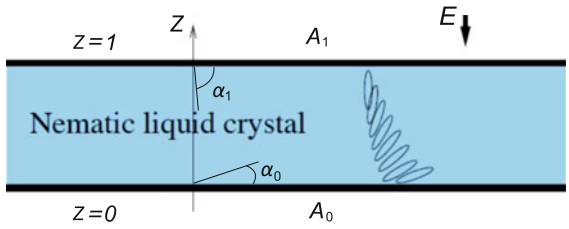

Fig. 1 Sketch showing setup and summarizing key parameters in dimensionless coordinates

applied electric field, will, however, change sign if the electric field direction is reversed. Since the representative parameter values listed above give $\Upsilon \approx 10$, we assign this value to Υ throughout our computations: $\Upsilon = 10$ henceforth.

The surface energy density models the preferred behavior of the molecules at each bounding surface. We use the formula proposed by Rapini and Papoular [22]. If $g^*_{\{0,h^*\}} = (K^*/h^*)g_{\{0,1\}}$ are the surface energies per unit length at the boundaries $z^* = 0,\ h^*$, then

$$g_{\{0,1\}} = \frac{\mathcal{A}_{\{0,1\}}}{2}\sin^2(\theta - \alpha_{\{0,1\}}) \quad \text{where} \quad \mathcal{A}_{\{0,1\}} = \frac{h^* A^*_{\{0,h^*\}}}{K^*}. \tag{5}$$

Here $A^*_{\{0,h^*\}}$ are the anchoring strengths at $z^* = 0,\ h^*$ and $\alpha_{\{0,1\}}$ are the preferred angles; as $A^* \to \infty$, the anchoring becomes strong, and the director angle is forced to take the value α. The sketch in Fig. 1 summarizes the setup and notation.

The total (dimensionless) free energy for the system is given by

$$J = \int_0^1 W(\theta, \theta_z)\,\mathrm{d}z + g_0(\theta)|_{z=0} + g_1(\theta)|_{z=1}\,,$$

and equilibrium solutions to the system are those functions $\theta(z)$ that minimize J. The standard calculus of variations approach, with $\theta(z) \mapsto \theta(z) + \epsilon\eta(z)(0 < \epsilon \ll 1)$, leads to $J \mapsto J[\theta + \epsilon\eta] = J[\theta] + \epsilon J_1 + \epsilon^2 J_2 + O(\epsilon^3)$, and for $\theta(z)$ to be a minimizer of J we require $J_1 = 0$, $J_2 > 0$, for all admissible variations η (the condition on J_2 ensures we have a minimum, rather than a maximum, of the free energy). After Taylor expansion, the expression for J_1 is found to be

$$J_1 = \int_0^1 \left(\eta W_\theta + \eta_z W_{\theta_z}\right)\mathrm{d}z + \eta g_{1\theta}|_{z=1} + \eta g_{0\theta}|_{z=0}\,.$$

A further integration by parts leads to

$$J_1 = \int_0^1 \eta\left(W_\theta - \left(W_{\theta_z}\right)_z\right)\mathrm{d}z + \eta(g_{1\theta} + W_{\theta_z})\big|_{z=1} + \eta(g_{0\theta} - W_{\theta_z})\big|_{z=0};$$

the condition that this must vanish for all admissible variations $\eta(z)$ leads to the usual Euler–Lagrange equation for θ, subject to boundary conditions on $z = 0,\ 1$:

$$W_\theta - \left(W_{\theta_z}\right)_z = 0, \qquad (g_{0\theta} - W_{\theta_z})\big|_{z=0} = 0, \qquad (g_{1\theta} + W_{\theta_z})\big|_{z=1} = 0. \tag{6}$$

We note that the second variation J_2 is easily calculated to be

$$2J_2 = \int_0^1 \{\eta^2[W_{\theta\theta} - (W_{\theta\theta_z})_z] + \eta_z^2 W_{\theta_z\theta_z}\}\,\mathrm{d}z + \eta^2(g_{1\theta\theta} + W_{\theta\theta_z})\Big|_{z=1} + \eta^2(g_{1\theta\theta} - W_{\theta\theta_z})\Big|_{z=0}, \tag{7}$$

so that the stability of any steady solutions calculated may be checked.

2.2 Time-dependent energetics: gradient flow

The weak form of the foregoing steady-state minimization may be written as

$$\langle W_\theta, \eta\rangle + \langle W_{\theta_z}, \eta_z\rangle + g_{1\theta}\eta|_{z=1} + g_{0\theta}\eta|_{z=0} = 0.$$

In reality, of course, if the system is not at equilibrium, then it will evolve over time toward a steady state described by the preceding equations. A truly accurate description of this dynamic process requires the full equations of nematodynamics [17,23], which couple flow to director reorientation. For our explorations of multidimensional parameter space that follow, however, this model is extremely computationally intensive, and instead we follow several other authors (e.g., Kedney and Leslie [24] and Davidson and Mottram [20]) in assuming that the system evolves in the direction that minimizes its total free energy (a gradient flow). Both bulk and surface components will evolve in this way, and this process may be represented as

$$\langle \tilde{\mu}\theta_t, \eta\rangle + \langle W_\theta, \eta\rangle + \langle W_{\theta_z}, \eta_z\rangle + [\tilde{\nu}\theta_t\eta + g_{1\theta}\eta]|_{z=1} + [\tilde{\nu}\theta_t\eta + g_{0\theta}\eta]|_{z=0} = 0,$$

where $\tilde{\mu}$ and $\tilde{\nu}$ may be interpreted as dimensionless bulk and surface rotational viscosities, respectively. With the natural choice of dimensionless time set by

$$t = t^* \frac{K^*}{\tilde{\mu}^* h^{*2}} \tag{8}$$

(where $\tilde{\mu}^*$ is the dimensional rotational viscosity of the NLC molecules, typically around 0.1 N s m^{-2}), $\tilde{\mu} = 1$. The integration by parts carried out above then leads to the evolution equation and boundary conditions

$$\theta_t + W_\theta - \left(W_{\theta_z}\right)_z = 0, \qquad (\tilde{\nu}\theta_t + g_{0\theta} - W_{\theta_z})\big|_{z=0} = 0, \qquad (\tilde{\nu}\theta_t + g_{1\theta} + W_{\theta_z})\big|_{z=1} = 0.$$

With bulk and surface energy densities given by (2), (5), this system becomes

$$\theta_t = \theta_{zz} - \mathcal{D}\sin 2\theta, \tag{9}$$

$$\tilde{\nu}\theta_t = \theta_z - \frac{\mathcal{A}_0}{2}\sin 2(\theta - \alpha_0) + \frac{\mathcal{F}}{2}\sin 2\theta \quad \text{on } z = 0, \tag{10}$$

$$-\tilde{\nu}\theta_t = \theta_z + \frac{\mathcal{A}_1}{2}\sin 2(\theta - \alpha_1) + \frac{\mathcal{F}}{2}\sin 2\theta \quad \text{on } z = 1, \tag{11}$$

with $\mathcal{D}$ (dimensionless dielectric coefficient), $\mathcal{F}$ (dimensionless field strength), and $\mathcal{A}_{\{0,1\}}$ (dimensionless surface energy) given by (3) and (5). This model is closed by specification of an initial condition $\theta(z, 0)$. When θ is independent of time, this is exactly the steady-state model (6).

Our strategy is to solve the steady-state model at zero field to find the two solutions of lowest energy, then use our time-dependent model (9)–(11) to investigate the conditions under which switching between the two steady states is possible, by application of a transient electric field. Until we take switching time into account as part of our device optimization (Sect. 4.4), the time of application of the field is fixed at $t = 25$ in our simulations; with the time scaling chosen in (8) above, and with representative values $\tilde{\mu}^* = 0.1$ N s m^{-2}, $K^* = 1.6 \times 10^{-11}$ N, $h^* = 10^{-6}$ m, this corresponds to dimensional time $t^* = 0.156$ s.

3 Bistability and switching

3.1 Stable, field-free steady states

The steady-state problem at zero field is particularly simple, reducing to

$$\theta_{zz} = 0, \qquad \theta_z = \pm\frac{\mathcal{A}_{\{0,1\}}}{2}\sin 2(\theta - \alpha_{\{0,1\}}) \quad \text{on } z = 0,\ 1.$$

Thus $\theta = az+b$, where the boundary conditions lead to coupled nonlinear equations for a and b. After simplification, two field-free solutions, which we call θ_1 and θ_2, are found:

$$\theta_1 = az + \frac{1}{2}\sin^{-1}\left(\frac{2a}{\mathcal{A}_0}\right) + \alpha_0,$$
$$\theta_2 = -az - \frac{1}{2}\sin^{-1}\left(\frac{2a}{\mathcal{A}_0}\right) + \alpha_0 + \pi,$$

where a must be found by numerically solving

$$a^2\left(1 + \frac{\mathcal{A}_1}{\mathcal{A}_0}\cos(2a + 2(\alpha_0 - \alpha_1))\right)^2 = \frac{\mathcal{A}_1^2}{4}\sin^2(2a + 2(\alpha_0 - \alpha_1)). \tag{12}$$

The solutions $\theta_{\{1,2\}}$ correspond to director fields $\boldsymbol{n}_{\{1,2\}} = (\sin\theta_{\{1,2\}}, 0, \cos\theta_{\{1,2\}})$. Equation (12) has multiple solutions for a in general, but in practice it is the smallest positive solution that gives the solutions $\boldsymbol{n}_{\{1,2\}}$ of lowest energy (the stablest solutions of the system).

3.2 Switching investigation

With two steady field-free solutions found, we may now address the dynamic problem of how we might switch from one to the other and back again by application of a transient electric field. That this is possible in certain parameter regimes was demonstrated by Cummings and Richardson [2], who studied a special case of the general model presented previously. They found that when the anchoring angles are $\pi/2$ out of phase ($\alpha_1 = \alpha_0 - \pi/2$) and the anchoring strengths are the same at both boundaries ($\mathcal{A}_1 = \mathcal{A}_0$), two stable steady field-free states of equal energy exist, and the states may be switched, reversibly, by application of a transient electric field. The two-way switching proved possible only for sufficiently small anchoring strength, however: in the case studied in [2] with $\alpha_0 = \pi/3$, switching was possible only when $\mathcal{A}_0 \lesssim 1.2$. This value may be rather small for robust device operation.[1]

Our strategy here is to consider the much more general model (9)–(11), with a specific "switching protocol": we suppose the system is in one of the two stable steady states at zero field and then apply a constant electric field for a time period t_1 before decreasing the field linearly and continuously to zero over a subsequent time period t_2. Mathematically, this means that we solve the system (9)–(11) with the initial condition $\theta(z, 0) = \theta_{\{0,1\}}(z)$ and with the variable field

$$\mathcal{F} = \mathcal{F}(t) = \begin{cases} \mathcal{F}_{\max} & 0 < t < t_1, \\ \dfrac{\mathcal{F}_{\max}}{t_2}((t_1 + t_2) - t) & t_1 < t < t_1 + t_2, \\ 0 & t > t_1 + t_2. \end{cases} \tag{13}$$

Once the field has been removed, we continue the computation until the new zero-field equilibrium is reached. By the comment following (3), the parameter $\mathcal{D}$ that appears in the governing equation (9) is given by $\mathcal{D} = \mathcal{F}^2/\Upsilon$ (for constant dimensionless material parameter $\Upsilon = 10$), so it is also a function of t. While we do not vary this basic switching protocol throughout our analysis, we consider $\mathcal{F}_{\max}$ and t_1 to be adjustable parameters, keeping the ratio t_1/t_2 fixed at 5. Following the justification given in Sect. 2, the anchoring strengths $\mathcal{A}_0$, $\mathcal{A}_1$, and the anchoring angles, α_0, α_1, are also taken as adjustable parameters. Switching occurs if the initial condition $\theta_{\{0,1\}}(z)$, by the end of the simulation, is transformed into $\theta_{\{1,0\}}(z)$. For a successful bistable device we require two-way switching.

[1] For example, as a minimum the surface anchoring must be strong enough that it is not disturbed by thermal fluctuations, yielding a condition $\mathcal{A} \gg k_B^* T^* h^*/(K^* S^*)$, where k_B^* is Boltzmann's constant, T^* is the absolute temperature of the system, and S^* is the effective cross-sectional area of the nematic molecule. Depending on the NLC used and the device size, this restriction can vary enormously, but for small NLC molecules it could be prohibitive.

3.3 Optimization

Since we know from the results of [2] that two-way switching of the proposed bistable device is possible, our focus here is on finding the "best" possible such device. The question of what is best is not easy to answer because a good bistable device should have several desirable properties. The properties we consider are as follows:

- The device should be robust. A key feature here is that the energy wells of the free energy minima should be reasonably deep. This includes the surface energy contributions; so the dimensionless surface energies $\mathcal{A}_{\{0,1\}}$ should not be too small. (The upper bound of 1.2 found in the previous analysis is likely prohibitively small; a device with such low surface energies could be prone to undesired switching, e.g., if the device was jolted.)
- Two-way switching should be possible at relatively low electric field strengths. Thus, given a value of the material parameter Υ, the value $\mathcal{F}_{\max}$ of the applied switching field should not be too large.
- The two steady states $\boldsymbol{n}_1$ and $\boldsymbol{n}_2$ should be optically distinct. Therefore, the two solutions found should be sufficiently "different" by some suitable measure, which we take as an approximation of the difference in optical transmission of the two states when the layer is placed between crossed polarizers.
- The time taken to switch from one stable state to the other should be as short as possible.

These conditions are conflicting, to a certain extent, so some design decisions must be made as to which are more important. The approach we take is to define a "benefit function" B, which takes account of each of the foregoing criteria. We define

$$B = \begin{cases} \min\{A_0, A_1\} + \mu C(\boldsymbol{n}_1, \boldsymbol{n}_2) - \nu|\mathcal{F}_{\max}| - \gamma(t_1 + t_2) & \text{if 2-way switching occurs,} \\ 0 & \text{otherwise,} \end{cases} \tag{14}$$

where $C(\boldsymbol{n}_1, \boldsymbol{n}_2)$ is a contrast function defined below, and we seek to maximize this function.[2] The first term in B ensures that surface energies will be as large as possible (subject to the other constraints), the second term maximizes the contrast between the two stable states found, the third term minimizes the field strength at which the two-way switching occurs, and the fourth term minimizes the length of time for which the electric field is applied.

The weight factors μ, ν, and γ are chosen at our discretion and allow for adjustment of the weight of each of the terms in B in order to emphasize different desired properties; for example, if fast switching is considered of paramount importance, then a large value for γ should be used. Optimization of B for given values of μ, ν, and γ is a computationally intensive process, requiring a search through $(\mathcal{A}_0, \mathcal{A}_1, \alpha_0, \alpha_1, \mathcal{F}_{\max}, t_1)$ parameter space (recall that we set $t_1/t_2 = 5$ throughout our simulations) in order to determine where two-way switching occurs and, if so, what the corresponding value of B is.

3.4 The contrast function $C(\boldsymbol{n}_1, \boldsymbol{n}_2)$

Our contrast function is based on the difference in optical transmission of our two solutions. Recall that we are solving for the director angle θ numerically in our time-dependent simulations, so that we obtain a discretized solution $\{\theta_j\}_{j=1}^N$ on our mesh of size N. For a given discretized solution we obtain the optical transmission between crossed polarizers as follows: the retardation δ for a given director configuration is defined by [25]

$$\delta = \frac{2\pi n_0}{\lambda_0} \int_0^h \frac{1}{\sqrt{1 - \frac{n_e^2 - n_o^2}{n_e^2} \sin^2\theta(z^*)}} - 1 \, \mathrm{d}z^*,$$

[2] Note: In principle the function B defined in (14) could assume negative values at some points of parameter space, in which case the value zero in its definition could easily be replaced by some suitable negative number. This did not occur in any of our simulations.

where n_o and n_e are the ordinary and extraordinary refractive indices and λ_0 the wavelength in vacuo. To obtain a somewhat more general expression for the contrast function (see below), we use the small birefringence approximation, $n_o/n_e - 1 \ll 1$, to evaluate δ for each steady state, which leads to

$$\delta \approx \frac{\varepsilon^2 \pi n_o h}{\lambda_0 N} \sum_{j=1}^{N} \sin^2 \theta_j, \quad \varepsilon^2 = 1 - \frac{n_o^2}{n_e^2}.$$

We then use this expression to evaluate the transmission T [25],

$$T = \sin^2(\delta/2),$$

and thence

$$T \approx \left(\frac{\varepsilon^2 \pi n_o h}{\lambda_0 N} \sum_{j=1}^{N} \sin^2 \theta_j \right)^2 = \text{constant} \times \left(\sum_{j=1}^{N} \sin^2 \theta_j \right)^2.$$

This approximation, while not as accurate as evaluating the transmission according to the exact definition, has the advantage that we do not need to specify the refractive indices when evaluating T, so the results are somewhat more general. Finally, then, in our numerical implementation, we define the contrast function $C(\boldsymbol{n}_1, \boldsymbol{n}_2)$ in (14) by the following expression, proportional to the difference in optical transmissions of the two states θ_1, θ_2:

$$C(\boldsymbol{n}_1, \boldsymbol{n}_2) = \left| \left(\sum_{j=1}^{N} \sin^2 \theta_{1,j} \right)^2 - \left(\sum_{j=1}^{N} \sin^2 \theta_{2,j} \right)^2 \right|.$$

4 Optimization: numerical method and results

As indicated previously, our task is to search through the parameter space $(\mathcal{A}_0, \mathcal{A}_1, \alpha_0, \alpha_1, \mathcal{F}_{\max}, t_1)$ of anchoring strengths, anchoring angles, switching field, and switching time to determine whether two-way switching occurs and, if it does, which point in parameter space maximizes the benefit function B defined in (14). Since the benefit function is time consuming to evaluate, and parameter space is large, we implement a simulated annealing method [26] to achieve the maximization. Due to the complexity of the full problem, we approach it in stages.

1. As a simple test case we first maximize B when $\nu = \gamma = 0$. We fix $\alpha_1 = \alpha_0 - \pi/2$ (but α_0 can vary); $|\mathcal{F}_{\max}|$ and t_1 are also fixed, but $\mathcal{F}_{\max}$ can be of either sign. Here the optimization is carried out in 3D $(\alpha_0, \mathcal{A}_0, \mathcal{A}_1)$ parameter space.
2. We next allow α_1 to vary independently and search optima in 4D $(\alpha_0, \alpha_1, \mathcal{A}_0, \mathcal{A}_1)$ parameter space.
3. Next, we allow $\nu > 0$ in B and minimize the switching field strength.
4. Finally, we allow $\gamma > 0$ and take switching time into account.

In all cases we use a simulated annealing method to maximize the benefit function B [26]. This is a gradient method with a certain stochastic character, represented by a "temperature". An initial simplex in parameter space is required to start the method [$(n + 1)$ initial points specified in an n-dimensional parameter space]. The system is "cooled" from an initial state, and the "temperature" at any stage captures the probability that the method can move down gradients in B (rather than always up gradients, as is the case for a standard simplex maximization method). At zero temperature the method has no stochastic element and is equivalent to the simplex method [26]. There is a certain amount of choice in the method's implementation: firstly in the choice of so-called annealing schedule (how the system is cooled) and secondly in the choice of initial simplex to start the method. To deal with the dependence on initial conditions, we perform the optimization for a random selection of initial simplices and make a histogram of the results. We plot the value of the benefit function attained for each implementation of simulated annealing (in an ideal implementation of simulated annealing this should always be the global optimum) against the number

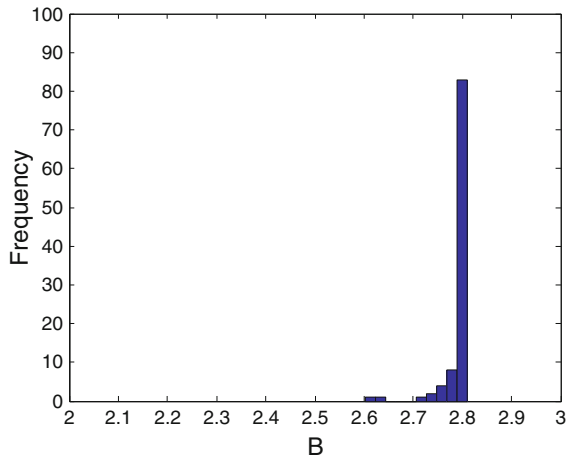

Fig. 2 *Histogram* showing optimization for benefit function B (14), with $\mu = 1.0$, $\nu = 0$, $\gamma = 0$, in 3D $(\mathcal{A}_0, \mathcal{A}_1, \alpha_0)$-parameter space for 100 different initial simplices. Note that the dominant spike in the value of B corresponds to the largest value attained

of initial simplices that converge to this value. The best results obtained are supposed to be the global optimum of B, and in general we see that this optimum corresponds to, or is close to, the dominant spike in the histogram, indicating reasonable robustness of the simulated annealing method. Regarding the annealing schedule, it is known that slower cooling produces more accurate results; however, it also increases the computational time. We carried out preliminary numerical experiments to find an annealing schedule that is accurate but that still allows us to obtain the results with reasonable use of computational resources.

4.1 Optimization: 3D results

In the simulations of Cummings and Richardson [2], the same model (9)–(11) was considered, with electric field specified by (13). However, in [2], a very limited device design was considered: it was assumed that (1) anchoring angles differ by $\pi/2$ ($\alpha_1 = \alpha_0 - \pi/2$); (2) α_0 was fixed at $\pi/3$; (3) surface energies were equal, $\mathcal{A}_1 = \mathcal{A}_0$; (4) the dimensionless switching field strength $|\mathcal{F}_{\max}|$ in (13) was fixed at 5; and (5) the dimensionless parameters t_1 and t_2 characterizing total switching time in (13) were fixed by $t_1 = 25$, $t_2 = 5$. Our first step toward generalizing and improving on these results is to allow different surface energies on each bounding surface and, while keeping $\alpha_1 = \alpha_0 - \pi/2$, allow the anchoring angle α_0 to vary freely. Other parameters are taken as listed above (see [2] for full details). We then seek to maximize the benefit function B as defined by (14) with $\nu = \gamma = 0$, as $\mathcal{A}_0$, $\mathcal{A}_1$, and α_0 vary. We carry out simulated annealing over this 3D parameter space as explained above, for 100 different (random) choices of initial simplex (4 starting points in $(\mathcal{A}_0, \mathcal{A}_1, \alpha_0)$-space).

The histogram of the results is shown in Fig. 2: from this we conclude that the optimum value of B here is approximately 2.82. It is possible in principle that different points in parameter space correspond to the same value of B, but it turns out that all 80-plus simulations that converge to this dominant optimum correspond to essentially the same parameter values: $\mathcal{A}_0 = 5.0$, $\mathcal{A}_1 = 2.4$, and $\alpha_0 = 1.36$. These values may be compared to the results of [2], where it was found that, with restrictions (1)–(5) outlined above, the largest value of $\mathcal{A}_0 = \mathcal{A}_1$ that permits two-way switching is 1.21, with $\alpha_0 = \pi/3 = 1.047$. Therefore, even this simple generalization has resulted in a twofold improvement in the operating values of surface energies, with associated implications for device robustness. For the simulations shown here, the parameter μ was chosen as $\mu = 1.0$; for this value the two nonzero terms in the benefit function B are approximately the same size and so are considered as being of roughly equal importance. We discuss the sensitivity to the choice of parameter μ in Sect. 4.2 below.

The switching simulations for the optimal parameter values found are shown in Fig. 3, for both cases $\boldsymbol{n}_1$ to $\boldsymbol{n}_2$, and vice versa. It appears that after application of the electric field the new "constant applied field" equilibrium state is obtained rapidly in both cases. This suggests that the field could be removed sooner and switching would still occur. However, numerical tests indicate that while this is possible for $\boldsymbol{n}_1$ to $\boldsymbol{n}_2$ switching, switching from state $\boldsymbol{n}_2$

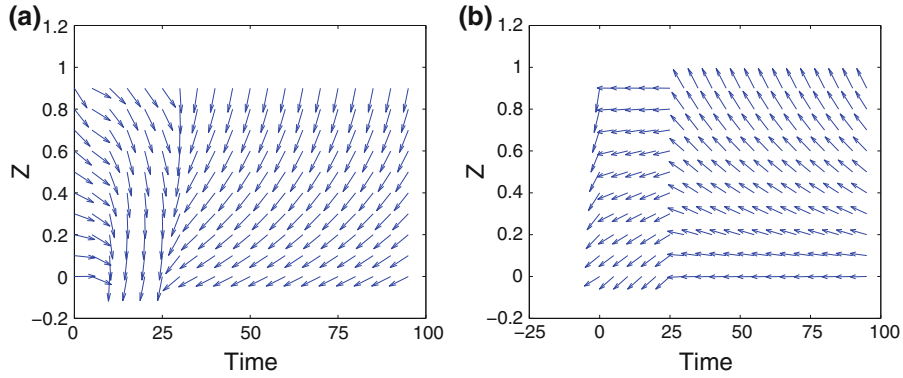

Fig. 3 Switching simulations $\boldsymbol{n}_1$ to $\boldsymbol{n}_2$ (**a**) and $\boldsymbol{n}_2$ to $\boldsymbol{n}_1$ (**b**) for the optimal benefit function parameters $\mathcal{A}_0 = 5.0$, $\mathcal{A}_1 = 2.4$ and $\alpha_0 = 1.36$. Dimensionless time runs along the horizontal axis, and the director field is displayed at equally spaced time intervals. The field is applied to $\boldsymbol{n}_1$ (or $\boldsymbol{n}_2$) at $t = 0$, maintained at a constant level until $t = 25$, and then decreased linearly to zero over the next five time units

to $\boldsymbol{n}_1$ is a more difficult process and is the limiting factor when minimizing total switching time (see Sects. 4.4 and 4.5 subsequently). We do not, in this paper, consider the more complicated (and impractical) scenario of allowing different switching protocols for the two switching directions (though in principle one could save energy by so doing).

4.2 Optimization: 4D results

The next step is to allow α_1 to vary independently of α_0 but keep other parameters fixed as outlined in Sect. 4.1. We again implement simulated annealing to maximize B, with $\nu = \gamma = 0$ in (14), but in 4D $(\mathcal{A}_0, \mathcal{A}_1, \alpha_0, \alpha_1)$-parameter space. The annealing method now requires five initial points (an initial simplex) in the 4D parameter space to begin the iteration; since results in general may depend on the choice of initial simplex, we use 100 different initial simplices as in Sect. 4.1 above and make a histogram of the results for the optimization in each case. The resulting histogram is shown in Fig. 4. There is more scatter in the optimization results this time, as we would expect in a larger parameter space; nonetheless, a clear optimum emerges, which is again the largest spike in the distribution. From these results we conclude that the optimum value of B here is about 3.55. Again, all optimization results that lie within the dominant spike are found to correspond to (more or less) the same point in parameter space: $\mathcal{A}_0 = 4.97$, $\mathcal{A}_1 = 3.20$, $\alpha_0 = 1.35$, and $\alpha_1 = -0.33$. Since the smaller surface energy is increased from the previous case above, we have improved robustness (as we would expect since we simply relaxed a constraint on the system). Switching simulations for the optimal parameter values are shown in Fig. 5.

Perhaps surprisingly, the key results do not appear to be very sensitive to the value chosen for μ (the weight associated with the contrast term in the benefit function). Table 1 shows how the optimal points in parameter space, and the corresponding value of the benefit function B, depend on the value of μ. Only the value of B changes significantly due to the direct appearance of μ in its definition. As μ varies by a factor of 4, the lower of the two surface energies varies by only a small amount in value. Therefore, we present only the histogram of results for the single value $\mu = 1.0$ in Fig. 4 (this is also the value of μ at which the two terms in B are roughly the same size). The value of μ is fixed at 1.0 for the remainder of the paper.

4.3 Optimization: 5D results, part 1

We now extend our investigation to allow the "switching field" $\mathcal{F}_{\max}$ to vary also; thus we allow $\nu > 0$ in the benefit function (14). This is the first stage at which we expect to see the effects of compromise in our optimization – since

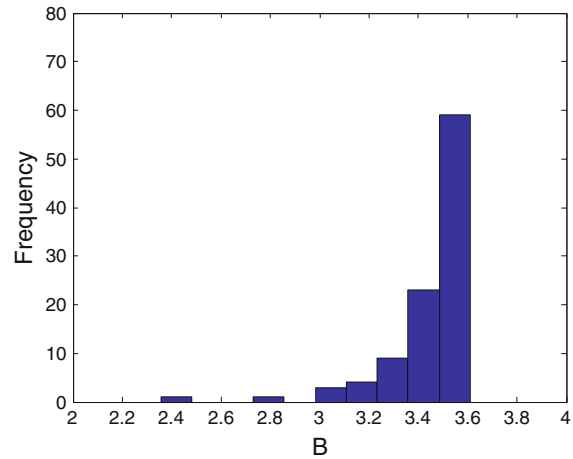

Fig. 4 *Histogram* showing optimization for benefit function B (14), with $\mu = 0.1$, $\nu = 0$, $\gamma = 0$, in 4D $(\mathcal{A}_0, \mathcal{A}_1, \alpha_0, \alpha_1)$-parameter space for 100 different initial simplices. Note that the dominant spike in the value of B corresponds to the largest value attained. Other spikes could be local optima

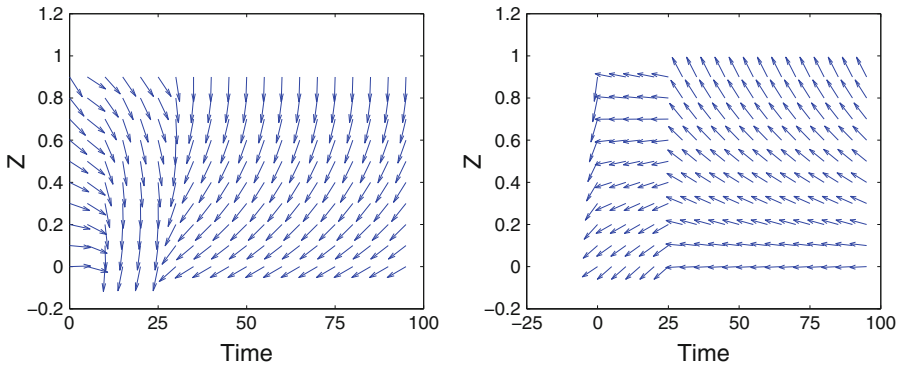

Fig. 5 Switching simulations $\boldsymbol{n}_1$ to $\boldsymbol{n}_2$ (left) and $\boldsymbol{n}_2$ to $\boldsymbol{n}_1$ (right) for the optimal benefit function parameters of Sect. 4.2, $\mathcal{A}_0 = 4.92$, $\mathcal{A}_1 = 3.20$, $\alpha_0 = 1.34$, and $\alpha_1 = -0.33$. Dimensionless time runs along the horizontal axis, and the director field is displayed at equally spaced time intervals. The field is applied to $\boldsymbol{n}_1$ (or $\boldsymbol{n}_2$) at $t = 0$, maintained at a constant level until $t = 25$, and then decreased linearly to zero over the next five time units

Table 1 Optimal parameter values and benefit function value as the weight μ is varied

μ	$\mathcal{A}_0$	$\mathcal{A}_1$	α_0	α_1	B
1.0	4.97	3.20	1.35	−0.33	3.61
2.0	4.83	3.18	1.34	−0.34	4.02
3.0	4.54	3.12	1.32	−0.35	4.45
4.0	4.27	3.05	1.31	−0.36	4.91

we now seek to decrease the size of the switching field, we may anticipate a corresponding decrease in the allowable surface energies at which switching can occur (a smaller field can generate less force on the NLC molecules; hence only weak anchoring can be broken).

Figure 6 shows the results of 100 simulated annealing computations to maximize B, with $\mu = 1.0$, $\nu = 0.1$, $\gamma = 0$ in (14). Figures 7 and 8 illustrate smaller ($\nu = 0.05$) and larger ($\nu = 0.3$) ν-values, respectively. The representative values of Fig. 6 were chosen, as before, so as to give an approximate balance between terms in the benefit function, "robustness," contrast, and low switching field all being considered of roughly equal importance. The left-hand subfigure in each case is the usual histogram of results (converged value of B versus frequency), while the right-hand subfigure shows a scatterplot of the corresponding switching field for each simulated annealing result, along with the corresponding surface energies $\mathcal{A}_0$ and $\mathcal{A}_1$. Note that the largest value of B obtained is, in all cases, no

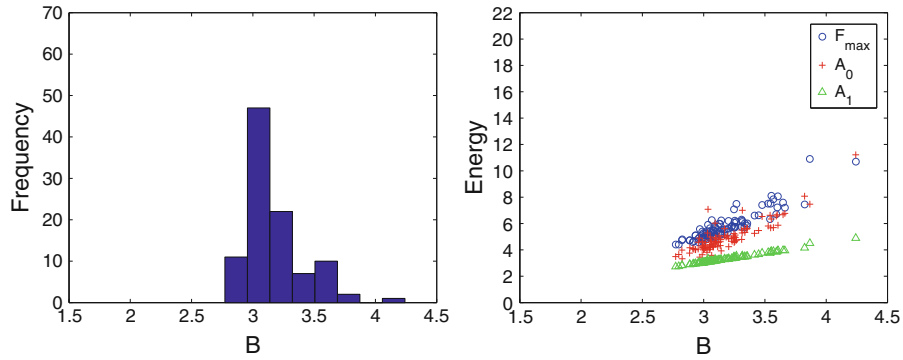

Fig. 6 Histogram of B-values and scatterplot of switching fields $|\mathcal{F}_{\max}|$ and associated surface energies from simulated annealing optimization of benefit function B (14), with $\mu = 1.0, \nu = 0.1, \gamma = 0$, in $(\mathcal{A}_0, \mathcal{A}_1, \alpha_0, \alpha_1, \mathcal{F}_{\max})$-parameter space. One hundred different initial simplices were used

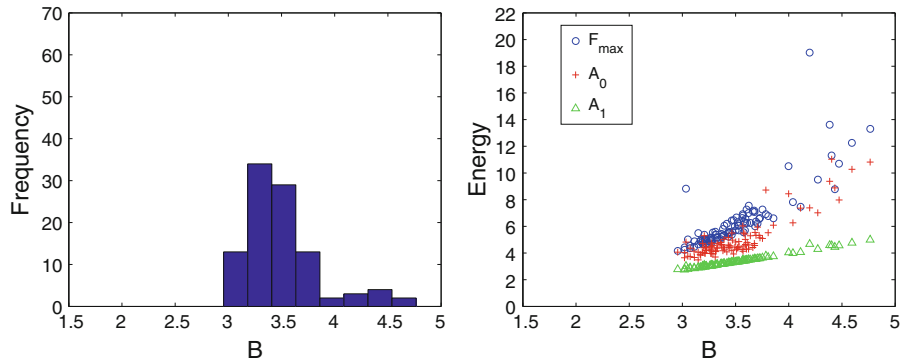

Fig. 7 As for Fig. 6 but with $\nu = 0.05$

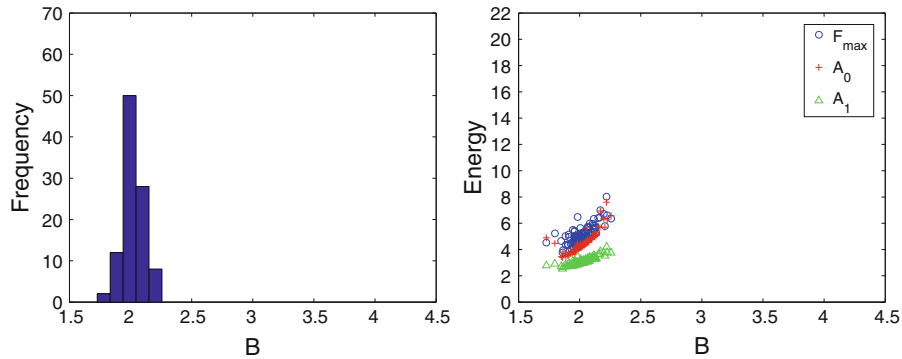

Fig. 8 As for Fig. 6 but with $\nu = 0.3$

longer the dominant spike in the histogram. The simulated annealing method is designed to converge to the global optimum of the given function and performed well in this regard for the 3- and 4D cases of Sects. 4.1 and 4.2; here it does less well and more often converges to suboptimum values of B. Since this increased scatter occurs for the benefit function, which, for the first time, includes competing effects, we conjecture that these competing terms lead to a much more complicated structure of the landscape defined by the benefit function, with several local optima, making the finding of global optima much more demanding. We expect in this case that implementing a sufficiently slow "cooling" schedule would allow us to converge to the global optimum more often; however, currently available

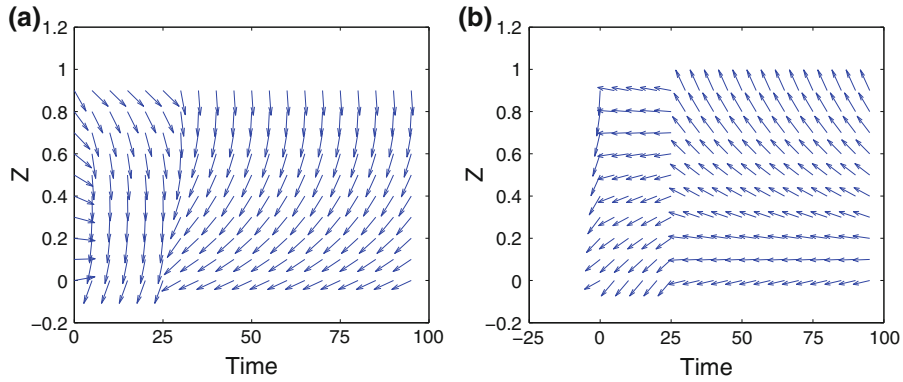

Fig. 9 Switching simulation (**a**) $\boldsymbol{n}_1$ to $\boldsymbol{n}_2$ and (**b**) $\boldsymbol{n}_2$ to $\boldsymbol{n}_1$, for optimal benefit function parameters for case $\mu = 1.0$, $\nu = 0.1$ ($\mathcal{A}_0 = 11.22$, $\mathcal{A}_1 = 4.89$, $\alpha_0 = 1.32$, $\alpha_1 = -0.35$, $\mathcal{F}_{\max} = -10.69$). Dimensionless time runs along *horizontal axis*, and the director field is displayed at equally spaced time intervals. The field is applied to $\boldsymbol{n}_1$ (or $\boldsymbol{n}_2$) at $t = 0$, maintained at a constant level until $t = 25$, and then decreased linearly to zero over the next five time units

computational resources do not allow us to explore this issue fully in such a large parameter space (we did repeat the simulations of Fig. 6 with a cooling schedule that was twice as slow, and obtained qualitatively very similar results, not reproduced here). Therefore, we compromise to a certain degree and assume that the data points in the rightmost spike of the histograms represent the global optimum of B, while other converged simulations represent local optima (it was verified directly for several cases that converged values of the benefit function are indeed local maxima).

As usual, what is of interest is not the numerical value of B when maximized, but the corresponding values of the optimal parameters; and as noted previously, with competing terms in the benefit function B we see evidence of multiple maxima. From the scatterplots in Figs. 6–8, for example, we see that, although it is a rare event, the simulated annealing algorithm can converge to the same value of B but with different switching fields $\mathcal{F}_{\max}$, corresponding to multiple device designs that (according to our chosen measure) are "equally optimal". Unsurprisingly, we find that the larger $\mathcal{F}_{\max}$ "optima" (local, not global) are associated with larger surface energies $\mathcal{A}_0$, $\mathcal{A}_1$, while smaller $\mathcal{F}_{\max}$ "optima" (again, nonglobal) are associated with smaller surface energies. These findings reflect the fact that, if we want a device with large surface energies, then we require a larger field to break the surface anchoring and switch; and conversely, if we want switchability at low fields, then anchoring strengths cannot be too large.

By changing the weight ν associated with the switching field in the benefit function (14) we can alter the results somewhat, though the same general conclusions emerge. Figures 7 and 8 show the results for smaller and larger values, $\nu = 0.05$ and $\nu = 0.3$, respectively. In the former case, less value is placed on having a low switching field, and we find that the simulated annealing tends to converge to B-values with higher fields $\mathcal{F}_{\max}$ and higher surface energies. In the latter case, the higher weight associated with $\mathcal{F}_{\max}$ says that low switching fields are valued more, and indeed, the simulated annealing now converges to B-values that are associated with significantly lower values of $\mathcal{F}_{\max}$ (though, of course, lower surface energies as well). All the scatterplots are shown on the same axes for ease of comparison.

Figure 9 shows the two-way switching simulations corresponding to the optimum value of B obtained from the scatterplot of Fig. 6. The left-hand subplot shows the switching $\boldsymbol{n}_1$ to $\boldsymbol{n}_2$, while the right-hand subplot shows the switching $\boldsymbol{n}_2$ to $\boldsymbol{n}_1$ for this optimum, as detailed in the caption.

4.4 Optimization: 5D results, part 2

The final consideration that we wish to take into account is the total time taken to switch. Since we observe that the NLC rapidly relaxes to a zero field equilibrium once the electric field is removed, we measure switching time simply by the time for which the electric field must be applied, and we seek to minimize this. In the first

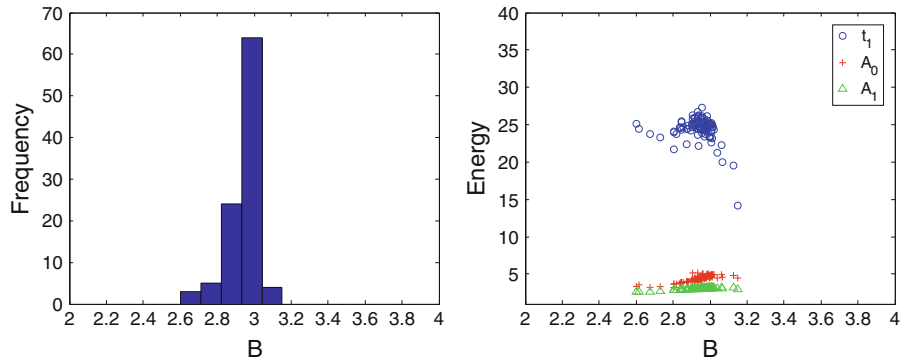

Fig. 10 Histogram of B-values and scatterplot of switching times t_1 and associated surface energies from simulated annealing optimization of benefit function B (14), with $\mu = 1.0$, $\nu = 0$, $\gamma = 0.02$, in 5D $(\mathcal{A}_0, \mathcal{A}_1, \alpha_0, \alpha_1, t_1)$-parameter space. One hundred different initial simplices were used

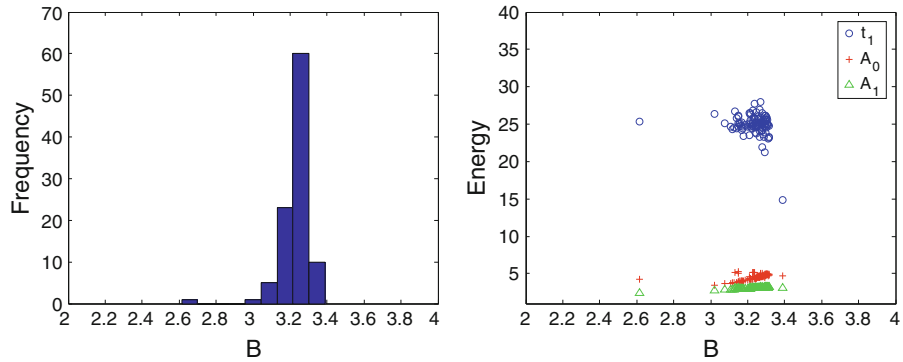

Fig. 11 As for Fig. 10 but with $\gamma = 0.01$

instance, we revert to the fixed-field-strength case, $|\mathcal{F}_{\max}| = 5$, and seek to optimize B (with $\nu = 0, \mu, \gamma > 0$) in $(\mathcal{A}_0, \mathcal{A}_1, \alpha_0, \alpha_1, t_1)$-parameter space. When doing so, the time t_2 over which the field is decreased to zero is fixed at $t_1/5$ in (13), consistent with the previous cases. Figure 10 shows the usual histogram of results and a scatterplot of switching times and surface energies for the results of 100 simulated annealing computations to maximize B, with $\mu = 0.1, \gamma = 0.02, \nu = 0$ in (14). Figures 11 and 12 illustrate smaller ($\gamma = 0.01$) and larger ($\gamma = 0.03$) γ-values, respectively. Again, these representative γ-values were chosen so as to give an approximate balance of terms in the benefit function. Once more, we see the possibility of multiple (local) maxima in the benefit function. In Fig. 10 we see an apparent global optimum, at the far right of the scatterplot. Two-way switching simulations for the parameters associated with this lowest-switching time solution are given in Fig. 13. As expected, the global optimum solution, though it has the shortest switching time ($t_1 = 14.15$), allows for higher surface energies than suboptimal solutions (local maxima of B). With the parameter values quoted at the end of Sect. 2.2 this corresponds to a dimensional switching time of around 88 ms, which, while rather slow for a conventional (high-power) LCD, is certainly competitive with the switching times of e-ink-based devices. Note also that this time could be reduced further by choosing a larger value for the parameter γ in the benefit function.

4.5 Optimization: 6D results

To take all the aforementioned effects into account simultaneously in our optimization, we must work with the full benefit function B with all parameters $\mu, \nu, \gamma \neq 0$ and maximize it in 6D $(\mathcal{A}_0, \mathcal{A}_1, \alpha_0, \alpha_1, \mathcal{F}_{\max}, t_1)$-parameter space.

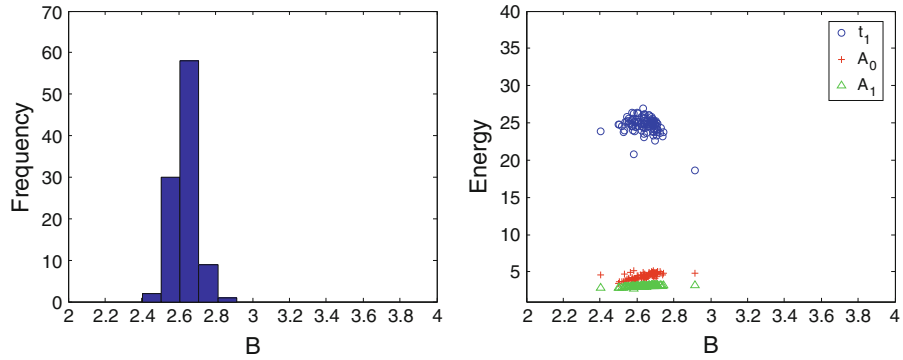

Fig. 12 As for Fig. 10 but with $\gamma = 0.03$

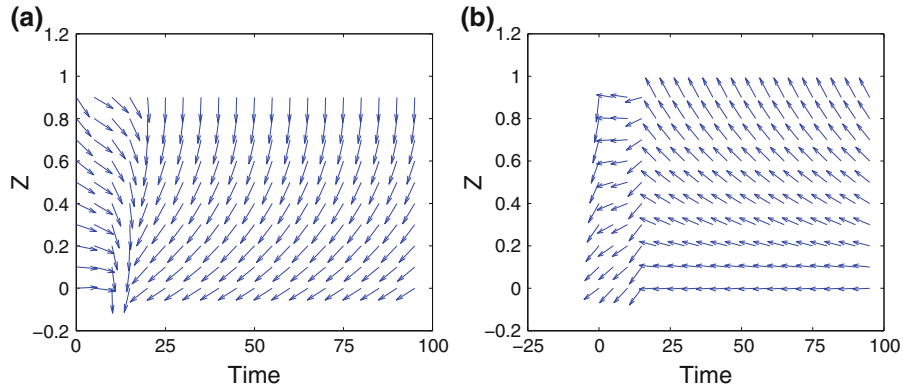

Fig. 13 Switching simulation (**a**) $\boldsymbol{n}_1$ to $\boldsymbol{n}_2$ and (**b**) $\boldsymbol{n}_2$ to $\boldsymbol{n}_1$ for optimal benefit function parameters for case $\mu = 1.0$, $\nu = 0$, $\gamma = 0.02$ ($\mathcal{A}_0 = 4.47$, $\mathcal{A}_1 = 3.04$, $\alpha_0 = 1.32$, $\alpha_1 = -0.34$, $t_1 = 14.15$). Dimensionless time runs along the *horizontal axis*, and the director field is displayed at equally spaced time intervals. The field is applied to $\boldsymbol{n}_2$ at $t = 0$, maintained at a constant level until $t = t_1$, and then decreased linearly to zero over the next $t_1/5$ time units

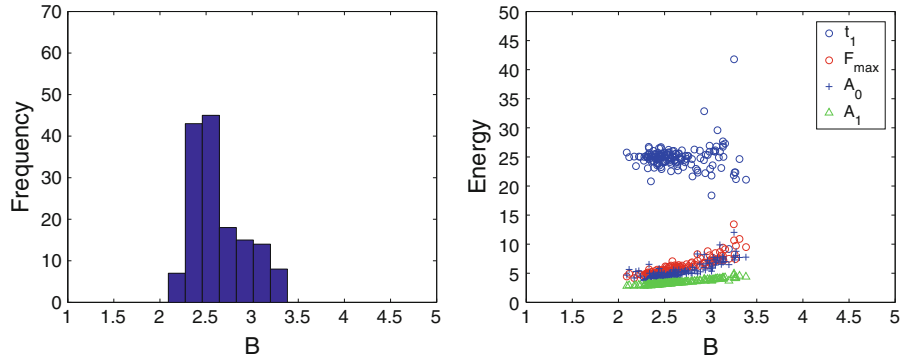

Fig. 14 *Histogram* of B-values and scatterplot of switching times t_1, switching fields $|\mathcal{F}_{\max}|$, and associated surface energies $\mathcal{A}_0$, $\mathcal{A}_1$ from simulated annealing optimization of benefit function B (14), with $\mu = 1.0$, $\nu = 0.1$, $\gamma = 0.02$, in 6D ($\mathcal{A}_0, \mathcal{A}_1, \alpha_0, \alpha_1, \mathcal{F}_{\max}, t_1$)-parameter space. One hundred fifty different initial simplices were used

As before, the results of the optimization will depend to a certain extent on the values chosen for μ, ν, and γ, and these values may be adjusted depending on the particular attributes we wish to emphasize. We present just one illustrative example here, with $\mu = 1.0$, $\nu = 0.1$, $\gamma = 0.02$. Figure 14 shows a histogram of results for the simulated annealing algorithm as applied to 150 different, randomly chosen, initial simplices in our 6D parameter

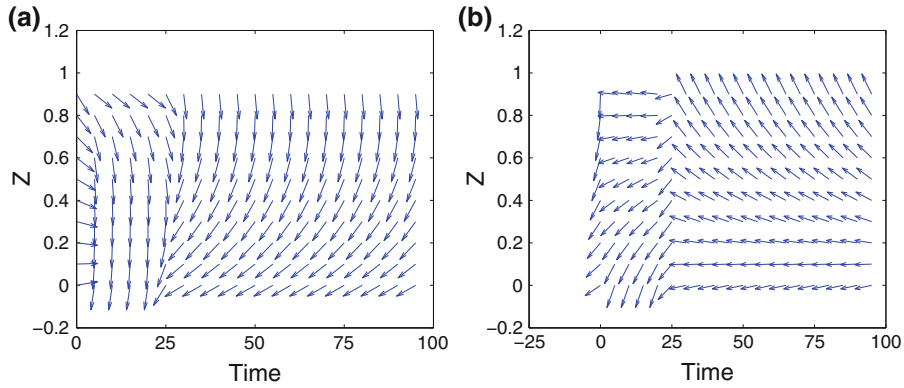

Fig. 15 Switching simulations $\boldsymbol{n}_1$ to $\boldsymbol{n}_2$ (**a**) and $\boldsymbol{n}_2$ to $\boldsymbol{n}_1$ (**b**) for optimal benefit function parameters for case $\mu = 1.0$, $\nu = 0.1$, $\gamma = 0.02$ ($\mathcal{A}_0 = 7.72$, $\mathcal{A}_1 = 4.54$, $\alpha_0 = 1.30$, $\alpha_1 = -0.37$, $\mathcal{F}_{\max} = -10.90$, $t_1 = 24.62$). Dimensionless time runs along the *horizontal axis*, and the director field is displayed at equally spaced time intervals. The field is applied to $\boldsymbol{n}_1$ (or $\boldsymbol{n}_2$) at $t = 0$, maintained at a constant level until $t = t_1$, and then decreased linearly to zero over the next $t_1/5$ time units

space, along with a scatterplot showing where in parameter space each of the converged simulated annealing results lies. We also present switching simulations $\boldsymbol{n}_1$ to $\boldsymbol{n}_2$ and $\boldsymbol{n}_2$ to $\boldsymbol{n}_1$ in Fig. 15, for the optimal parameter values found (corresponding to the largest value of B in Fig. 14, $B \approx 3.45$).

5 Discussion and conclusions

We have presented a study of a very simple bistable nematic liquid crystal display (LCD) device, consisting of a nematic sandwich, bounded by planar surfaces at which anchoring properties can be controlled. Regarding these anchoring properties (anchoring angles and anchoring strengths) as independent design parameters, we posed the question: which set of anchoring properties gives the "best" such device? Formulating and answering this question mathematically are the basis of this paper.

Several criteria were taken into consideration when deciding what makes a "good" device. From the point of view of design, a device is specified by choices of anchoring angles α_0, α_1, anchoring strengths $\mathcal{A}_0$, $\mathcal{A}_1$, and the material parameter $\Upsilon = \mathcal{F}^2/\mathcal{D}$ defined in (4). As a minimum, a workable device must be switchable (both ways) for some choice of applied electric field and manufacturable at physically attainable values of α_0, α_1, $\mathcal{A}_0$, $\mathcal{A}_1$, and Υ. A good device should have several additional desirable properties however, chiefly those listed in Sect. 3.3. To optimize these desirable properties, we introduced our benefit function B, defined in (14), and searched through the space of workable devices to maximize B.

Given the properties we wish to optimize simultaneously, it is natural that some tradeoff is necessary. This becomes particularly apparent when we carry out the optimization in stages, introducing one desirable quantity at a time. When we optimize only by maximizing the allowable surface energies (with implications for device robustness) and the optical contrast, dimensional surface energies that are both in excess of $3.2 \times K^*/h^*$ (where $K^* = K_1^* = K_3^*$ is the elastic energy of the liquid crystal and h^* is the thickness of the liquid crystal layer in the proposed device) are attainable. With representative values $K^* = 1.6 \times 10^{-11}$ N, $h^* = 10^{-6}$ m, this corresponds to a surface energy of $A^* = 5.1 \times 10^{-5}$ N m^{-1}, a fairly respectable value in terms of manufacturing attainability and robustness of the steady states to shocks. However, when we also consider minimizing the switching field (measured by the dimensionless quantity $\mathcal{F}_{\max}$) or the switching time, the allowable surface energies fall, to an extent that depends on how much weight we attach to each desirable property. Figures 6–8 and 10–12 exemplify this tradeoff, showing clearly that higher surface energies require higher switching fields in general and longer switching times.

The methods used here should be regarded as a tool to guide the design of a device that can be optimized for a choice of different effects. If a manufacturer is more concerned with switching at low fields, then our methods can

be used to optimize the proposed device with a relatively large value of the weight ν. Likewise, if higher surface energies are the primary concern, then small values of ν and γ should be chosen. Many other features that might be desirable in a device could, of course, similarly be incorporated into the benefit function using the approach of this paper; our benefit function is intended to be largely illustrative.

Of course, the proposed device is represented here by an idealized mathematical model, and we would not expect our results to be quantitatively correct in an experimental setup. Further work is needed to fine-tune the model. In particular, the assumptions that the electric field within the device is uniform and that the two elastic constants K_1^* and K_3^* are equal are not quantitatively correct. We are currently working on a refined model (steady state in the first instance) in which we solve for the electric field $\boldsymbol{E} = \nabla\phi$ within the sample, instead of assuming it to be uniform. While a time-dependent version of such a model can be formulated, a degree of quantitative uncertainty will persist since, while the gradient-flow arguments of Sect. 2.2 can be extended to the new coupled Euler–Lagrange equations for the director angle θ and electric potential ϕ, the time scales of the relaxation of θ and ϕ will be different, and we do not know precisely how they will differ.

We are also investigating the effect of variations parallel to the bounding surfaces that might give an improved device. Such variations could include gradients in surface energy (imparted by chemical treatments, for instance, or UV irradiation), variable anchoring angle (similar treatments), or variable surface topography. Our future research efforts will be focused on these areas in order to make our predictions more quantitative and directly applicable [27].

Acknowledgments This work was supported by the NSF under Grants DMS-0908158 and DMS-1211713, and by KAUST under Award No. KUK-C1-013-04. The authors would like to acknowledge informative and useful discussions with P. Palffy-Muhoray and colleagues from the Liquid Crystals Institute, Kent State University; with P. D. Howell, A. Majumdar and colleagues at the Oxford Centre for Collaborative and Applied Mathematics; and helpful comments from anonymous referees.

References

1. Kosc TZ (2005) Particle display technologies become E-Paper. Opt Photonics News 16(2):18–23
2. Cummings LJ, Richardson G (2006) Bistable nematic liquid crystal device with flexoelectric switching. Euro J Appl Math 17:435–463
3. Chen T-J, Chu K-L (2008) Pretilt angle control for single-cell-gap transflective liquid crystal cells. Appl Phys Lett 92(9):091102
4. Cui L, Jin W, Liu Y, Xie P, Zhang R, Zhu C, Wang C (1999) A combined method based on rubbing and UV-irradiation for preparing stable alignment layers with high pretilt angles. Mol Cryst Liquid Cryst 333:135–144
5. Hwang J-Y, Lee SH, Paek SK, Deo D-S (2003) Tilt angle generation for nematic liquid crystal on blended homeotropic polyimide layer containing trifluoromethyl moieties. Jpn J Appl Phys 42(1):1713–1714
6. Kim K-H, Baek J-I, Cheong B-H, Choi H-Y, Shin ST, Kim JC, Yoon T-H (2010) Pretilt angle control and multidomain alignment of liquid crystals by using polyimide mixed with liquid crystalline prepolymer. Appl Phys Lett 96(21):213507
7. Lee H-J, Kang D, Clark CM, Rosenblatt C (2009) Full control of nematic pretilt angle using spatially homogenous mixtures of two polyimide alignment materials. J Appl Phys 105(2):023508
8. Reznikov Y, Petschek RG, Rosenblatt C (1996) Magnetic field-mediated alignment of a nematic liquid crystal at a polymer surface exposed to ultraviolet light. Appl Phys Lett 68(16):2201–2203
9. Seo D-S (1999) Generation of high pretilt angle and surface anchoring strength in nematic liquid crystal on a rubbed polymer surface. J Appl Phys 86(7):3594–3597
10. Seo D-S (2000) Anchoring strength and high pretilt angle in nematic liquid crystal on rubbed organic solvent polyimide surfaces with trifluoromethyl moieties. J Korean Phys Soc 36(1):29–33
11. Vaughn KE, Sousa M, Kang D, Rosenblatt C (2007) Continuous control of liquid crystal pretilt angle from homeotropic to planar. Appl Phys Lett 90(19):194102
12. Wu W-Y, Wang C-C, Fuh AY-G (2008) Controlling pre-tilt angles of liquid crystal using mixed polyimide alignment layer. Opt Express 16(21):17131–17137
13. Yeung FS-Y, Xie F-C, Wan JT-K, Lee FK, Tsui OCK, Sheng P, Kwok H-S (2006) Liquid crystal pretilt angle control using nanotextured surfaces. J Appl Phys 99(12):124506
14. Komitov L, Barbero G, Dahl I, Helgee B, Olsson N (2009) Controllable alignment of nematics by nanostructured polymeric layers. Liquid Cryst 36(6):747–753
15. Lin C-J, Hong G-T, Pan R-P (2009) Alignment control of rubbed polyimide layers by UV-irradiation. Mol Cryst Liquid Cryst 512:911937–911945
16. Chandrasekhar S (1992) Liquid crystals, 2nd edn. Cambridge University Press, New York

17. DeGennes PG, Prost J (1993) The physics of liquid crystals, 2nd edn. International series of monographs on physics, vol 83. Oxford Science Publications, New York
18. Stewart IW (2004) The static and dynamic continuum theory of liquid crystals. Taylor & Francis, London
19. Blinov LM, Kolovsky M, Nagata T, Ozaki M, Yoshino K (1999) Influence of guest conformation (rod- or banana-like photo-isomers) on flexoelectric coefficients in nematic liquid crystals. Jpn J Appl Phys 38:L1042–L1045
20. Davidson AJ, Mottram NJ (2002) Flexoelectric switching in a bistable nematic device. Phys Rev E 65:051710
21. Murthy PRM, Raghunathan VA, Madhusudana NV (1993) Experimental determination of the flexoelectric coefficients of some nematic liquid crystals. Liquid Cryst 14:483–496
22. Rapini A, Papoular M (1969) Distorsion d'une lamelle nématique sous champ magnétique. Conditions d'ancrage aux parois. J Phys (Paris) Colloq 30(C4):54–56
23. Leslie FM (1979) Theory of flow phenomena in liquid crystals. Adv Liquid Cryst 4:1–81
24. Kedney PJ, Leslie FM (1998) Switching in a simple bistable nematic cell. Liquid Cryst 24(4):613–618
25. Yeh P, Gu C (2010) Optics of liquid crystal displays. Wiley, New Jersey
26. Press WH, Teukolsky SA, Vetterling WT, Flannery BP (1996) Numerical recipes in Fortran 90, 2nd edn. Cambridge University Press, New York
27. Choi M-C, Kim Y, Ha C-S (2008) Polymers for flexible displays: from material selection to device applications. Prog Polym Sci 33(6):581–630